Supplementary Information

Modelling algorithm for amorphous covalent triazine-based polymers

Ce Song,[ac] Fangyuan Hu,*[b] Zhaoliang Meng,[a] Shengming Li,[d] Tianpeng Zhang,[b] Wenlong Shao,[c] Siyang Liu,[b] and Xigao Jian*[abc]

[a] *School of Mathematical Sciences, Dalian University of Technology, No.2 Linggong Road, Gaoxin District, Dalian, Liaoning, China. E-mail: jian4616@dlut.edu.cn*

[b] *School of Materials Science and Engineering, State Key Laboratory of Fine Chemicals, Dalian University of Technology, No.2 Linggong Road, Gaoxin District, Dalian, Liaoning, China. E-mail: hufangyuan@dlut.edu.cn*

[c] *State Key Laboratory of Fine Chemicals, Liaoning Province Engineering Research Centre of High Performance Resins, Dalian University of Technology, No.2 Linggong Road, Gaoxin District, Dalian, Liaoning, China.*

[b] *School of Innovation and Entrepreneurship, Dalian University of Technology, No.2 Linggong Road, Gaoxin District, Dalian, Liaoning, China*

Table of content

1. Details of modelling algorithm and simulation method.

The starting configurations for modelling the atomistic CTF-type networks are generated by the Amorphous Cell module in BIOVIA Materials Studio 2017R2. 300 nitrile monomers are randomly packed into a cubic simulation cell at an initial density of 0.4 g/cm^3 under periodic boundary conditions. The relatively low initial density is selected because it may be beneficial for the pore formation.[1]

After the initial simulation box is established, the linking cycles are switched on to search for the potential cyano groups satisfied the bonding criteria. If the three potential cyano groups are detected in the current simulation box, single bonds will be added between the C and N atoms in the cyano groups to form the triazine rings in the manner displayed in Fig. 2. And the triple bonds in the initial cyano groups will be modified by double bonds. Moreover, the force field types of the related atoms need further adjustment according to the chemical structures and the applied force field. Then, an immediate geometry optimization is performed to optimize the local structure near the newly formed triazine ring. If no cyano groups in the simulation box satisfy the bonding criteria, a short NVT MD simulation (namely md1 type MD simulation in Fig. S1) will be performed to refresh the simulation box for another search attempt. This search manner is iterated until the satisfied cyano groups are detected or the maximum number of searching attempts (i.e., 50 in this study) is reached. Furthermore, an NVT MD simulation is conducted after each creation of three triazine rings. The linking cycles are iteratively performed until the desired number of triazine rings is successfully formed or maximum searching attempts for potential cyano groups arrive. This manner is analogous to the Polymatic code embedded in pysimm package[2] and has been successfully implemented on other CTF-type polymers in previous work[3]. The desired number of formed triazine rings is assigned as 200 herein because the number of cyano groups in the initial simulation box is 600 in this work.

After the accomplishment of linking cycles, the “unreacted” monomers remained in the simulation box are removed, and a compression and relaxation scheme (described in Table S1) is implemented to further optimize and equilibrate the network. The iterative linking cycles are conducted by an in-house Python script, and the automatic searching process for the potential cyano groups and aforementioned alterations of the networks during and at the end of linking cycles are implemented by in-house Perl scripts. The aforementioned in-house scripts are available from the correspondence author upon request.

Geometry optimizations and MD simulations in this work are carried out in the Forcite module in BIOVIA Materials Studio 2017R2 with COMPASS II force field.[4] Geometry optimizations performed after the formation of triazine rings consist of 1000 steps with fine quality settings and smart algorithm for energy minimization calculations. The NVT MD simulations conducted during the linking cycles utilize the Nosé-Hoover thermostat with a time step of 1 fs at 900 K, which is close to the experimental temperature. The md1 type NVT MD simulations (Fig. S1) comprise 5000 steps, and the md2 type NVT MD simulations (Fig. S1) consist of 10000 steps. The MD simulations performed in the gradual compression and relaxation scheme (Table S1) employ the Nosé-Hoover thermostat and Berendsen barostat with a time step of 1 fs. In addition, the van der Waals interactions are calculated by atom-based summation methods, and the cutoff distance used for geometry optimizations and MD simulations during the linking cycles is 5 Å, while 15 Å is utilized for the MD simulations performed in the gradual compression and relaxation scheme. Electrostatic interactions are evaluated by the Particle-Particle Particle-Mesh (PPPM) method with fine quality settings. Note that the aforementioned parameters have been successfully implemented in previous study.[3]

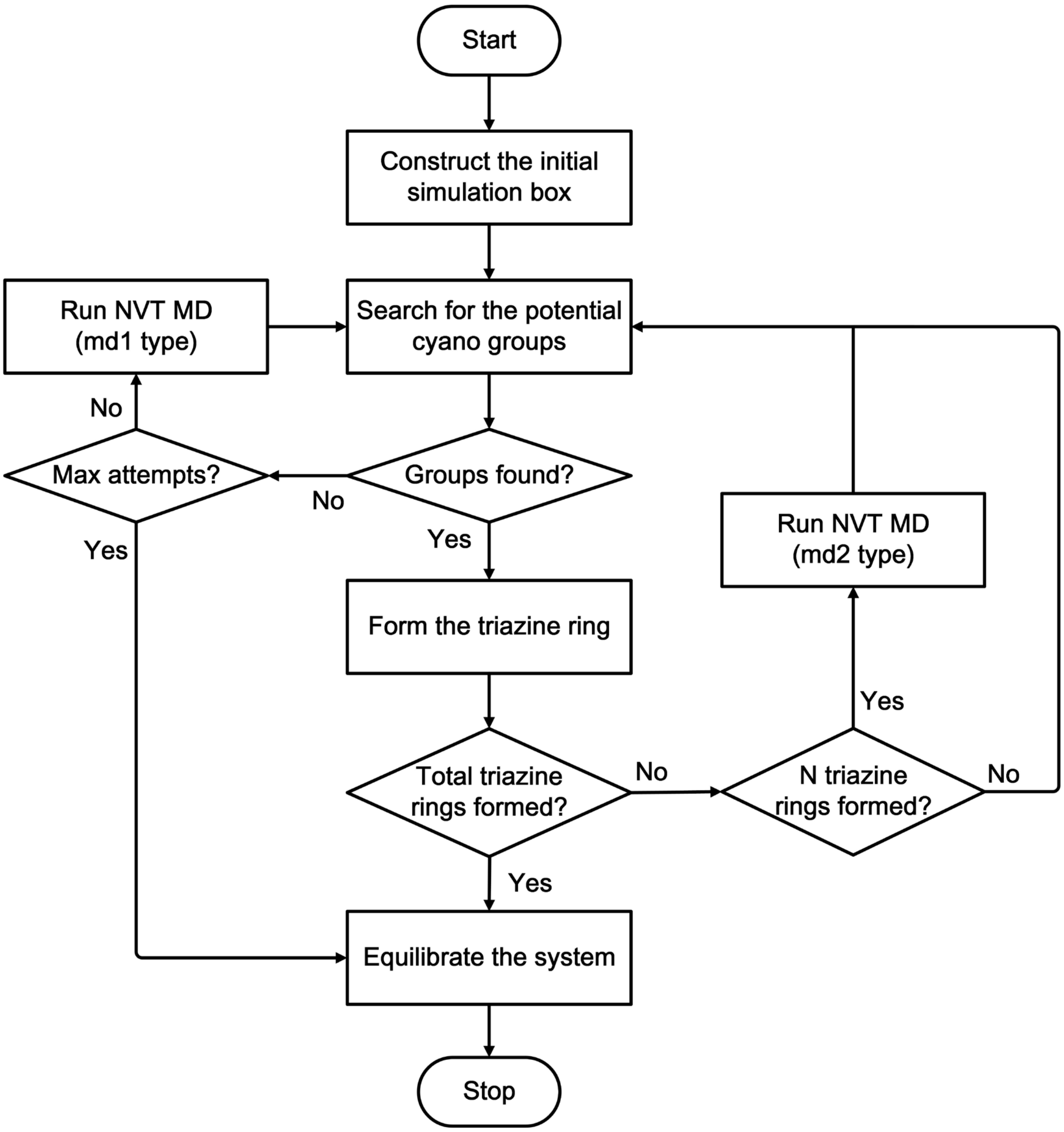

Fig. S1 Flowchart of the modelling algorithm.

Table S1 Gradual Compression and Relaxation Scheme

Step	Ensemble	Conditions	Length (ps)
1	NVT	300 K	500
2	NPT	300 K, 1 bar	50
3	NVT	300 K	500
4	NPT	300 K, 1 bar	50
5	NVT	300 K	500
6	NPT	300 K, 1 bar	2000
7	NVT	300 K	2000

2. Additional results for bonding criteria analysis.

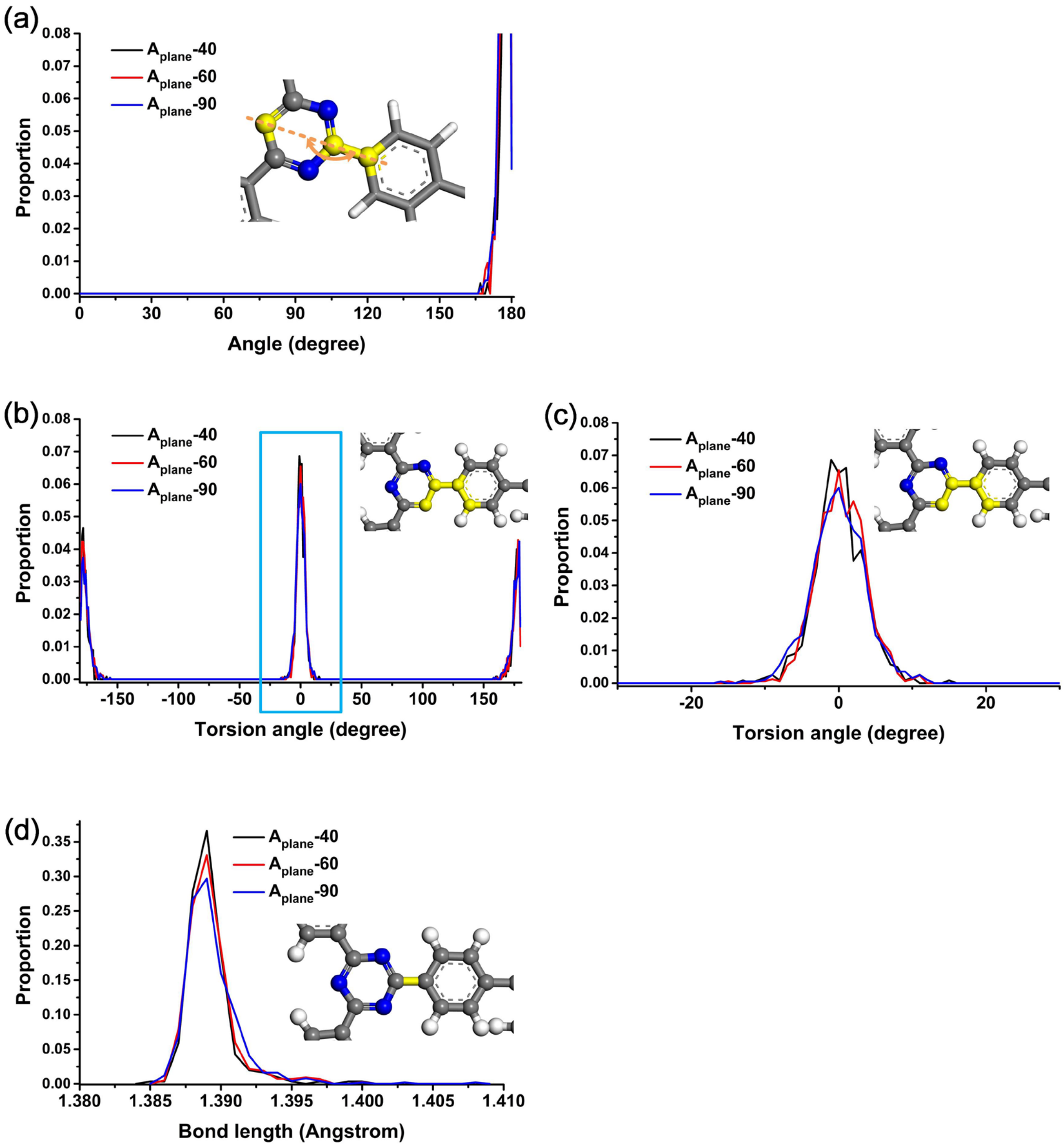

Fig. S2 Distributions of angles and bond lengths in the simulated models established by modelling algorithms with changing parameter of A_{plane}. (a) Full distribution of the angle depicted in the subplot; (b) full distribution of the torsion angle defined by the four atoms highlighted in yellow in the subplot; (c) partial distribution of the torsion angle for the range labeled by the blue box in panel (b); (d) length distribution of the bond highlighted in yellow in the subplot. The suffix “-x” in the legend specifies the permitted range size of A_{plane}.

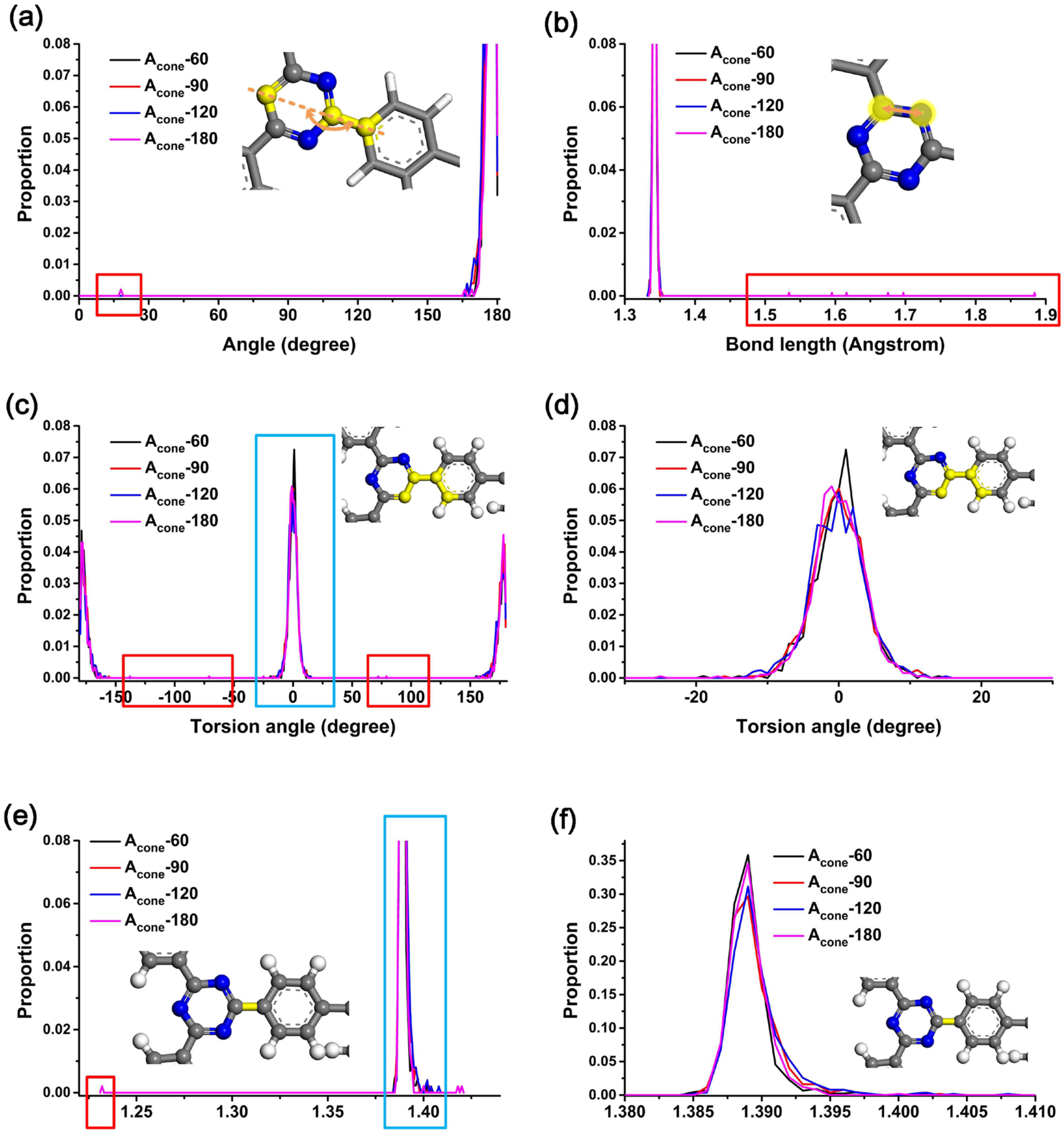

Fig. S3 Distributions of angles and bond lengths in the simulated models established by modelling algorithms with changing parameter of A_{cone}. (a) Full distribution of the angle depicted in the subplot; (b) full length distribution of the bond depicted in the subplot; (c) full distribution of the torsion angle defined by the four atoms highlighted in yellow in the subplot; (d) partial distribution of the torsion angle for the range labeled by the blue box in panel (c); (e) full length distribution of the bond highlighted in yellow in the subplot; (f) partial bond length distribution for the range labeled by the blue box in panel (e). The suffix "-x" in the legend specifies the permitted range size of A_{cone}. The red boxes mark the abnormal values for angles and bond lengths which imply the unrealistic structures remained in the networks that cannot be adequately optimized by the implemented geometry optimization steps during the linking cycles.

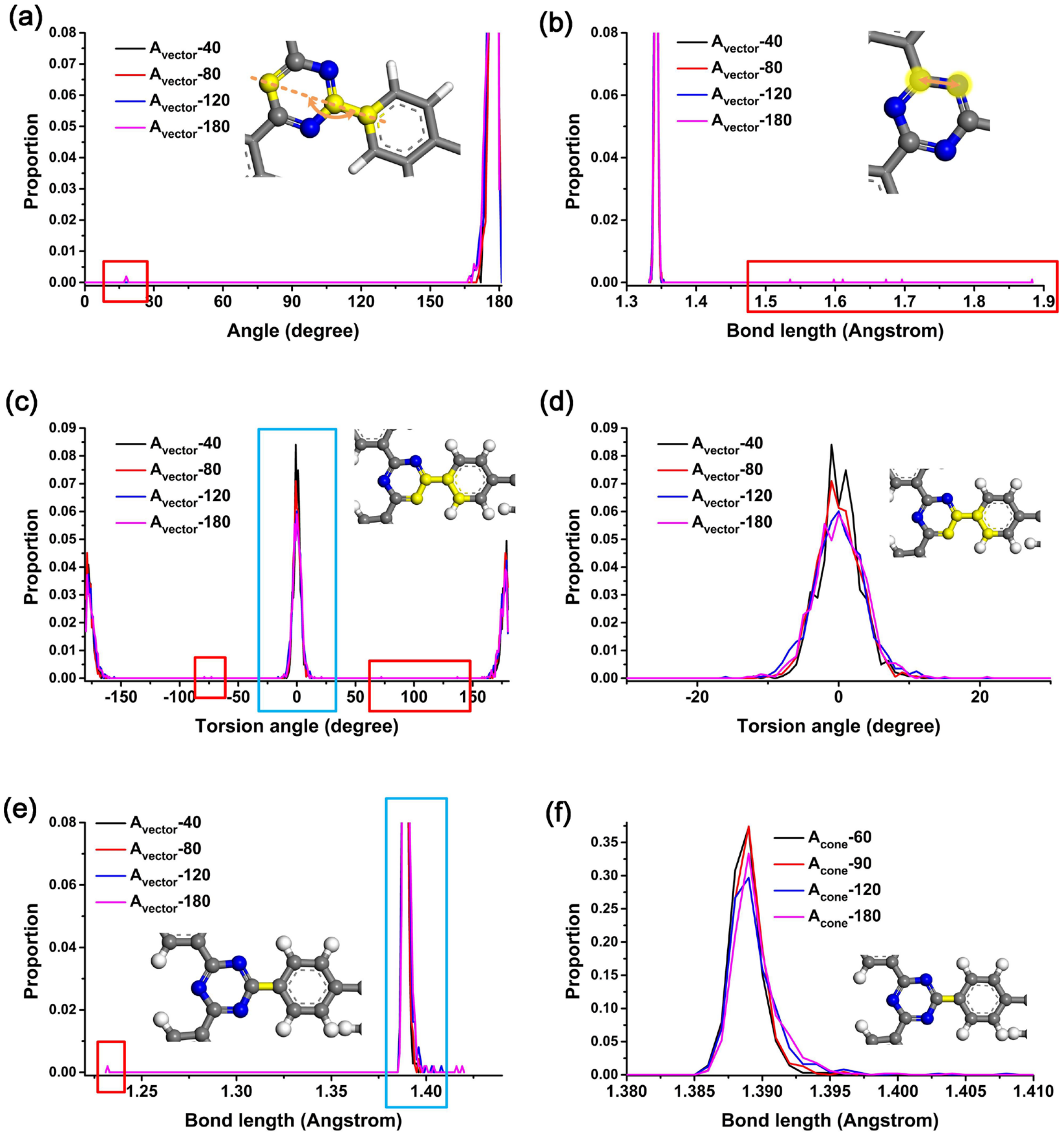

Fig. S4 Distributions of angles and bond lengths in the simulated models established by modelling algorithms with changing parameter of A_{cone} (a) Full distribution of the angle depicted in the subplot; (b) full length distribution of the bond depicted in the subplot; (c) full distribution of the torsion angle defined by the four atoms highlighted in yellow in the subplot; (d) partial distribution of the torsion angle for the range labeled by the blue box in panel (c); (e) full length distribution of the bond highlighted in yellow in the subplot; (f) partial bond length distribution for the range labeled by the blue box in panel (e). The suffix “-x” in the legend specifies the permitted range size of A_{vector}. The red boxes mark the abnormal values for angles and bond lengths which imply the unrealistic structures remained in the networks that cannot be adequately optimized by the implemented geometry optimization steps during the linking cycles.

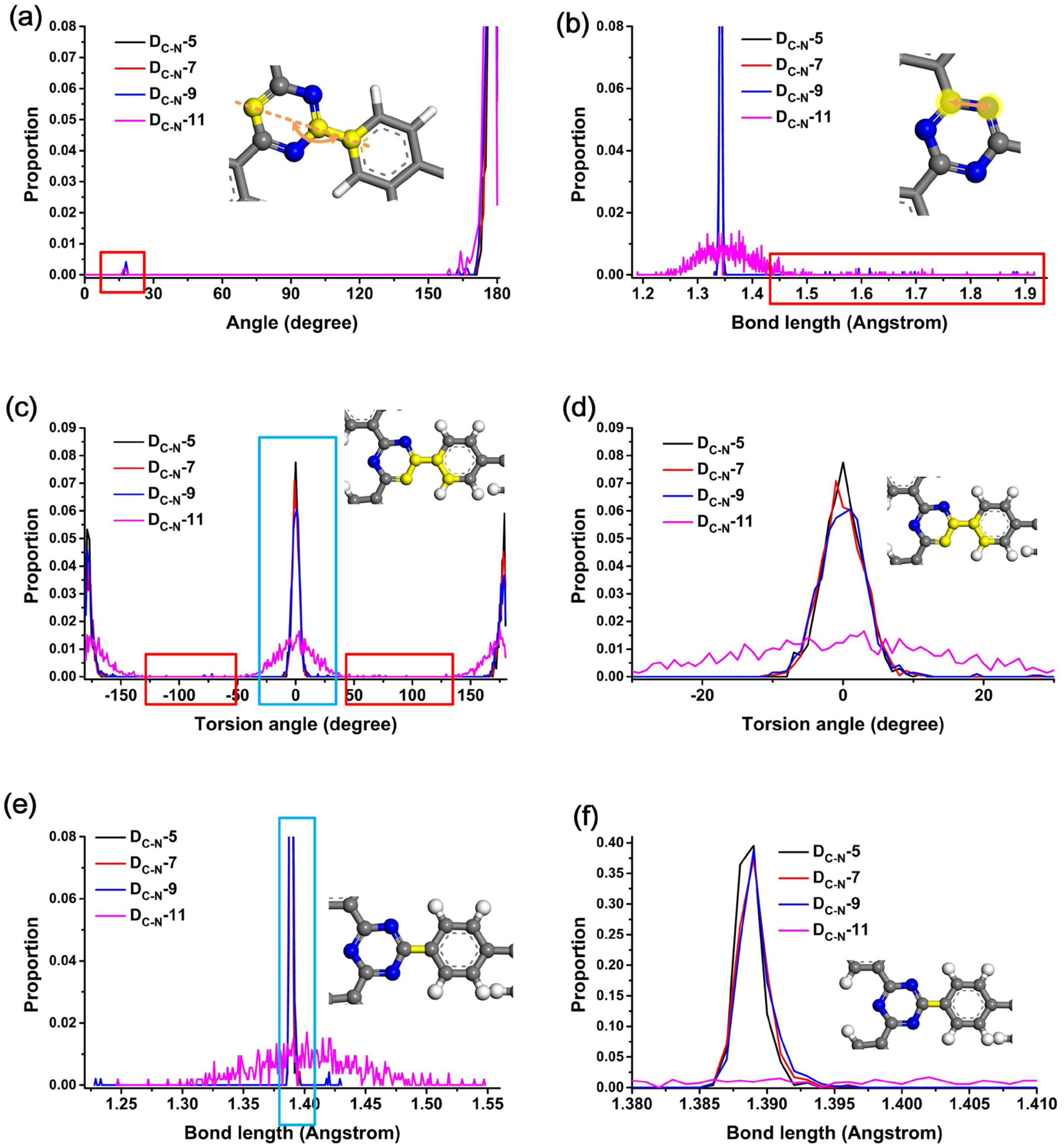

Fig. S5 Distributions of angles and bond lengths in the simulated models established by modelling algorithms with changing parameter of D_{C-N}. (a) Full distribution of the angle depicted in the subplot; (b) full length distribution of the bond depicted in the subplot; (c) full distribution of the torsion angle defined by the four atoms highlighted in yellow in the subplot; (d) partial distribution of the torsion angle for the range labeled by the blue box in panel (c); (e) full length distribution of the bond highlighted in yellow in the subplot; (f) partial bond length distribution for the range labeled by the blue box in panel (e). The suffix “-x” in the legend specifies the permitted range size of D_{C-N}. The red boxes mark the abnormal values for angles and bond lengths which imply the unrealistic structures remained in the networks that cannot be adequately optimized by the implemented geometry optimization steps during the linking cycles.

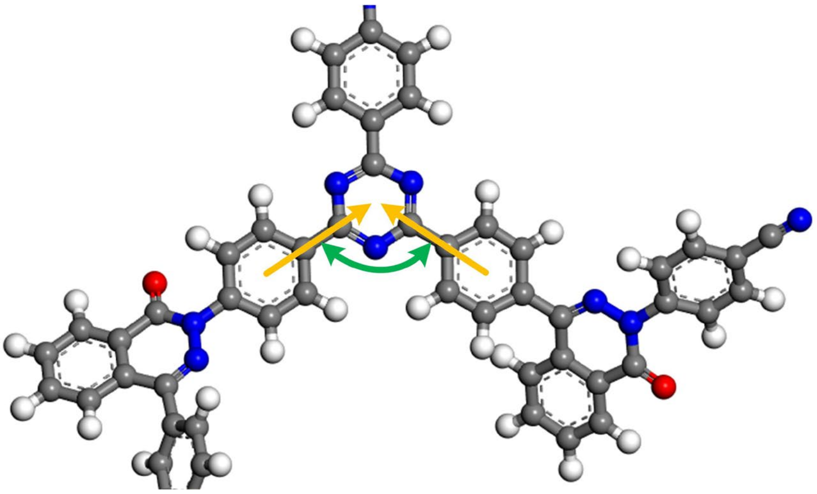

Fig. S6 Snapshot of the local structure around the formed triazine ring for MPCF-2 in the equilibrium state.

3. Simulation details for the pore size distribution.

The pore size distributions (PSDs) of the simulated models were calculated with zeo++ software[5, 6]. The kinetic radius of nitrogen molecules, that is, 1.82 Å, is assigned for the probe radius because the experimental PSD originates from nitrogen sorption measurements.

4. Supplementary structural properties of MPCF-2 models.

Table S2 Efficiency assessment on modelling algorithm applied for MPCF-2

	Formation Percentage (%)	Degree of Polymerization (%)	Average Attempts
MPCF-2a	77.50	96.67	3.4
MPCF-2b	76.00	95.00	3.9
MPCF-2c	77.00	95.00	2.9
MPCF-2d	77.00	96.33	3.1
MPCF-2e	71.00	94.67	2.2

[1] MPCF-2a-e represent the five independent models of MPCF-2 constructed by the proposed modelling algorithm.

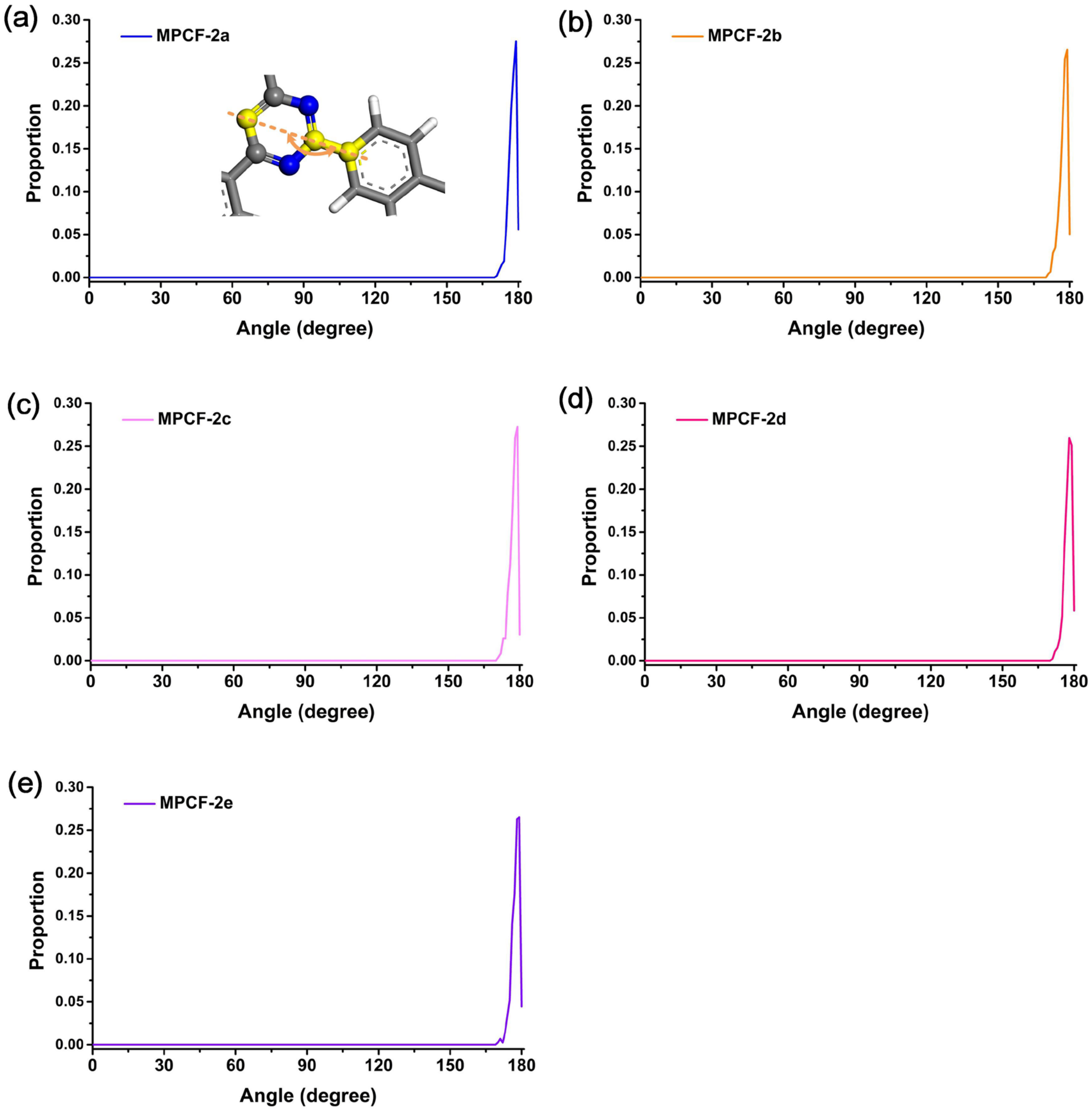

Fig. S7 Distributions of the angle depicted in the subplot for five independent MPCF-2 models, namely, MPCF-2a-e.

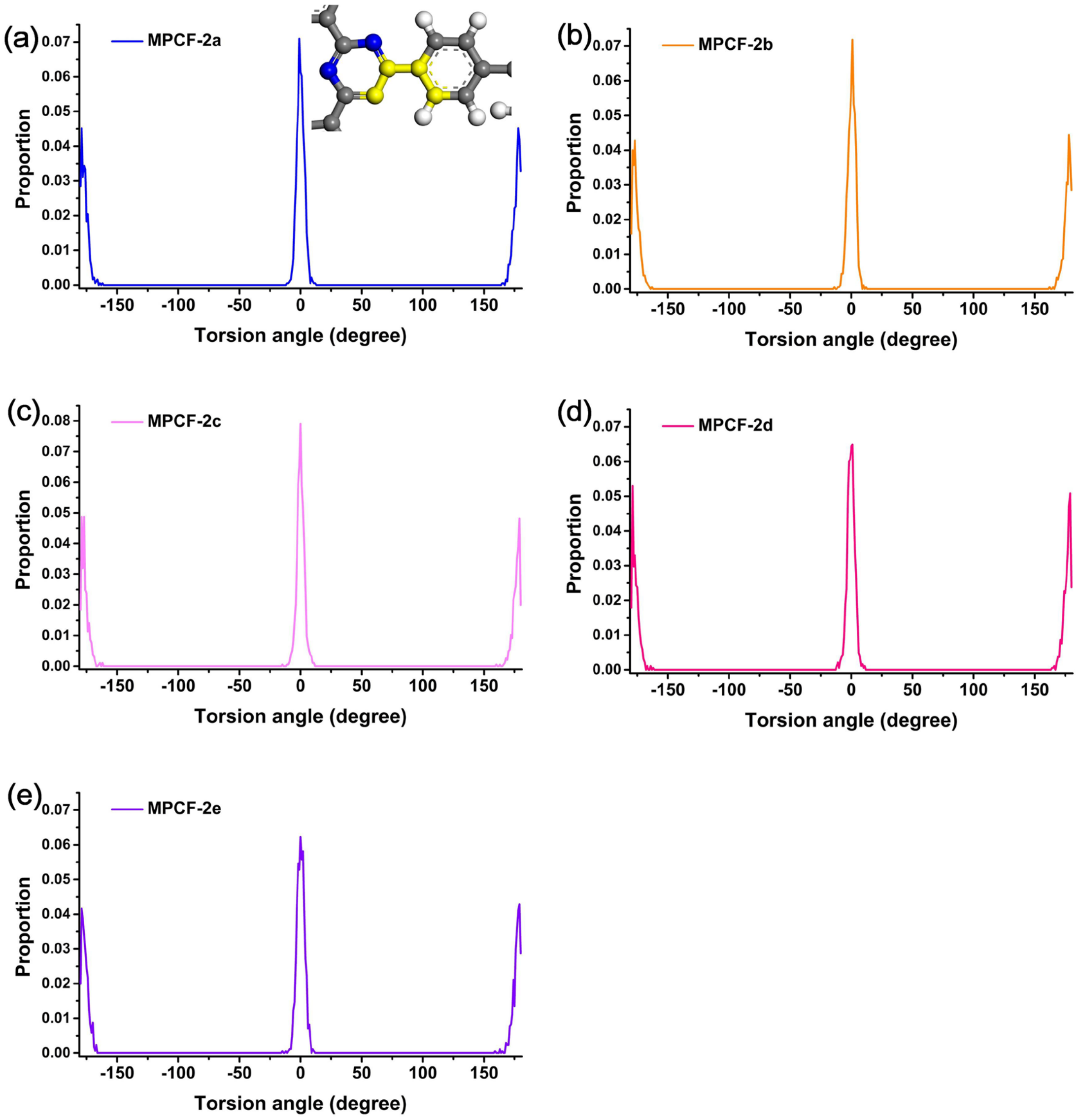

Fig. S8 Distributions of the torsion angle defined by the four atoms highlighted in yellow in the subplot for five independent MPCF-2 models, namely, MPCF-2a-e.

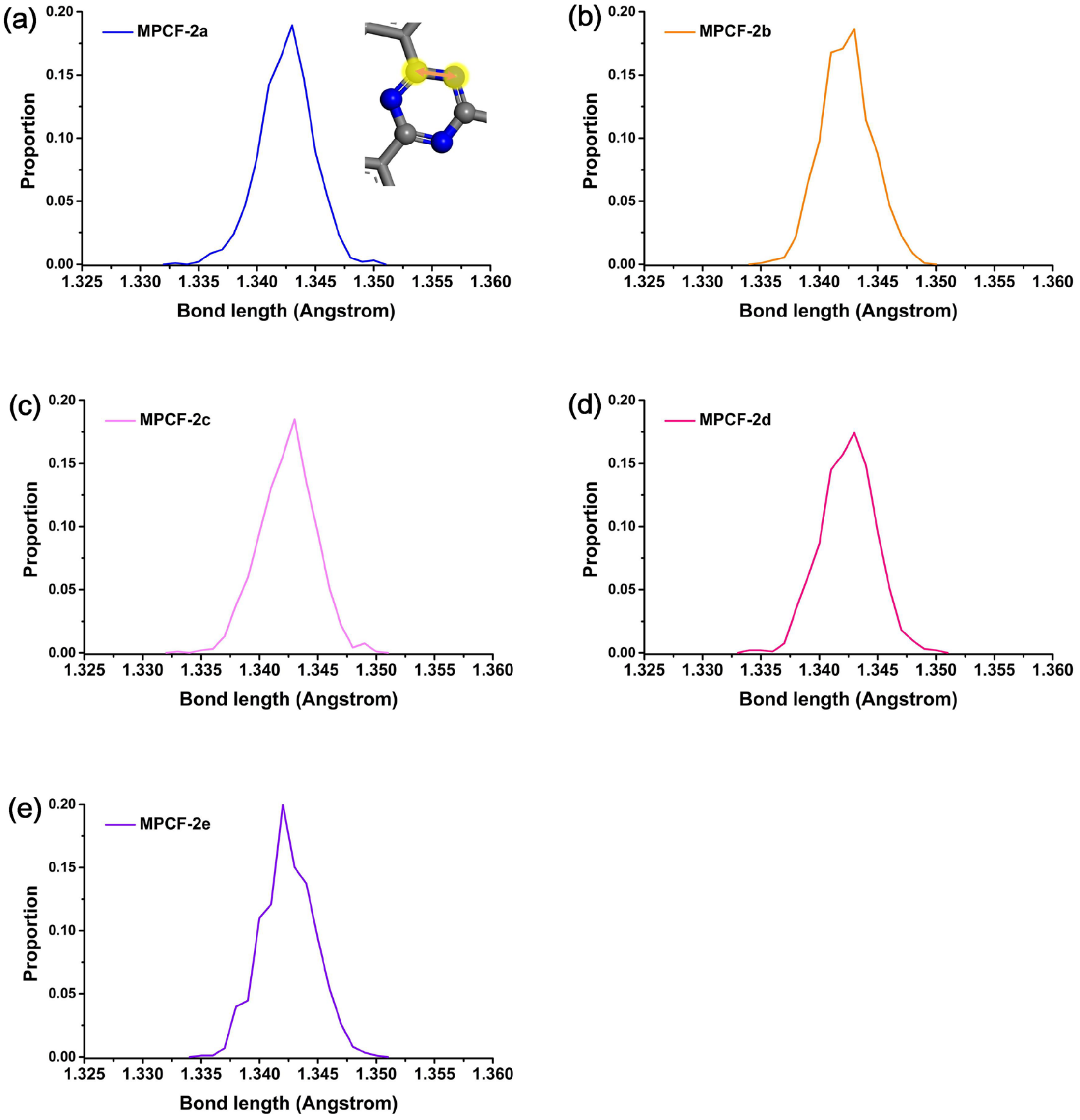

Fig. S9 Length distributions of the specific bond displayed in subplot for five independent MPCF-2 models, namely, MPCF-2a-e.

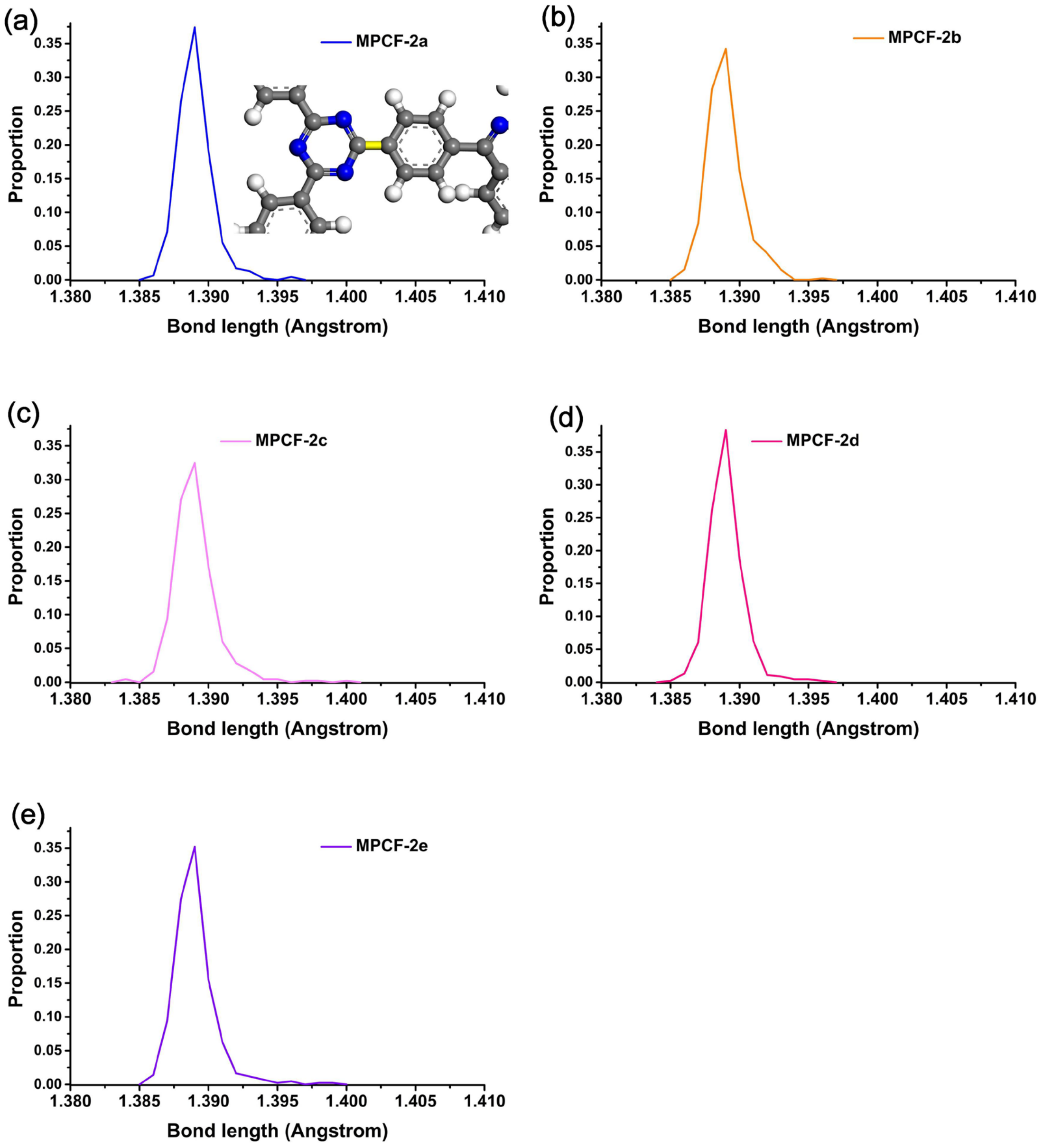

Fig. S10 Length distributions of the bond displayed in subplot for five independent MPCF-2 models, namely, MPCF-2a-e.

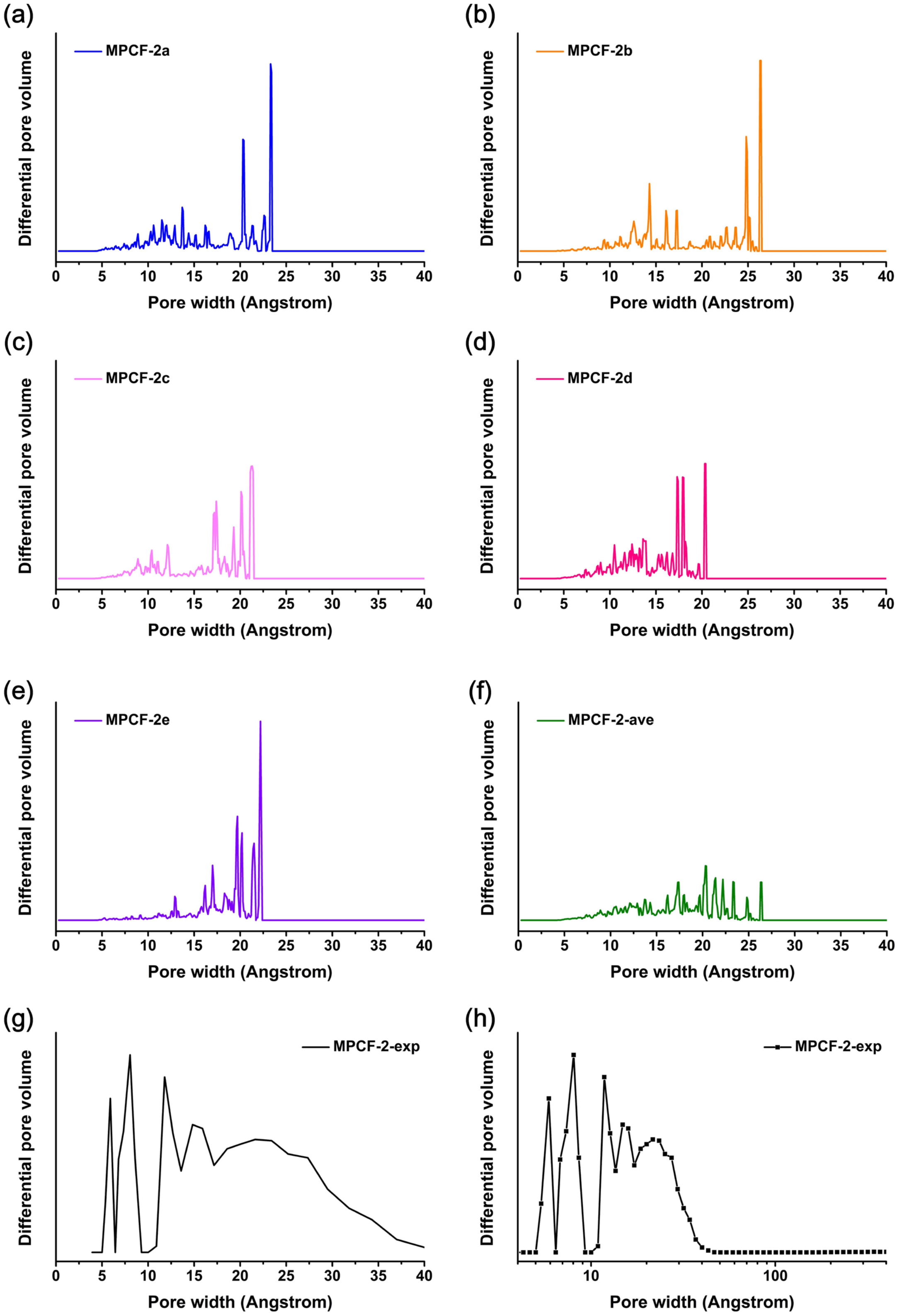

Fig. S11 (a-e) Simulated pore size distributions for the five independent MPCF-2 models, namely, MPCF-2a-e. (f) Average simulated pore size distribution for MPCF-2 models. (g, h) Experimental pore size distributions for MPCF-2 sample of different ranges for pore width.

5. Simulation details for the structure factors.

The structure factors of the simulated models were calculated by the ISSAC software[7] with periodic boundary conditions. The structure factor S(q) is interpreted by the following equation:

$$S(q) = 1 + 4\pi\rho \int_0^\infty r^2 \frac{sinqr}{qr}(g(r) - 1)dr, \qquad (1)$$

where g(r) represents the radial distribution function. g(r) was calculated by 1000 steps with a smoothing factor of 0.1.

6. Supplementary information for simulated MPCF-3 model.

Table S3 Efficiency assessment on modelling algorithm applied for MPCF-3

	Formation Percentage (%)	Degree of Polymerization (%)	Average Attempts
MPCF-3	70.5	93.67	4.4

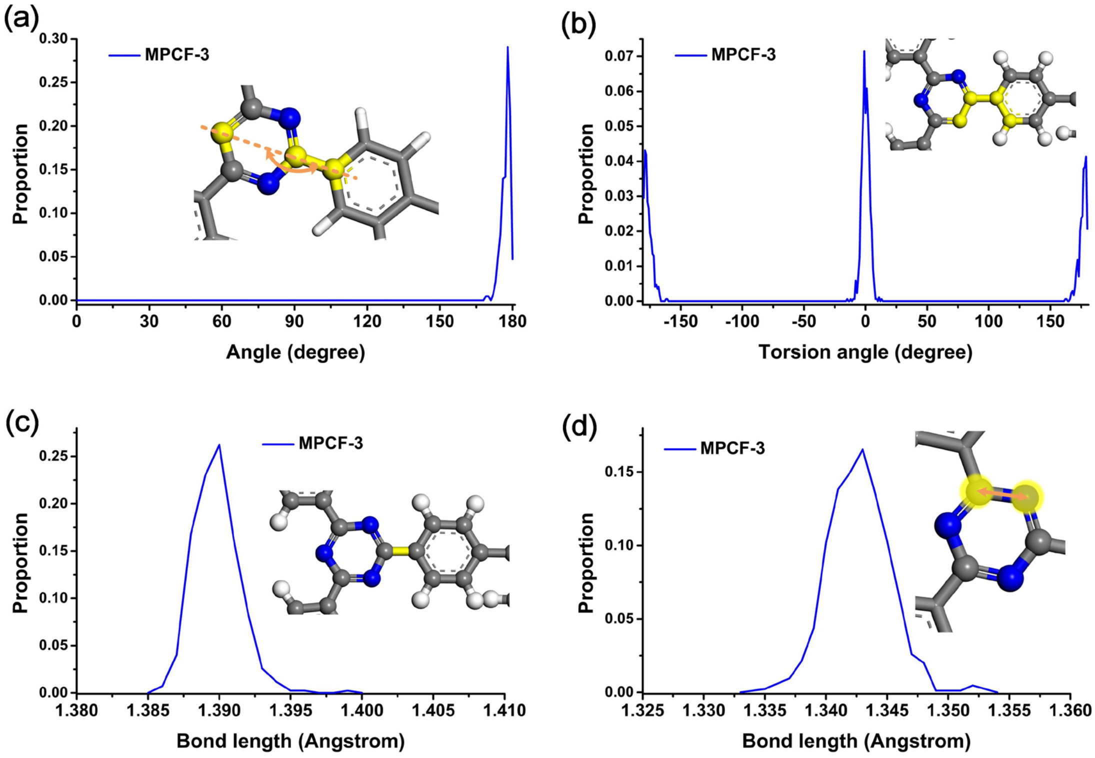

Fig. S12 Distributions of particular angles and bond lengths defined in the corresponding subplots.

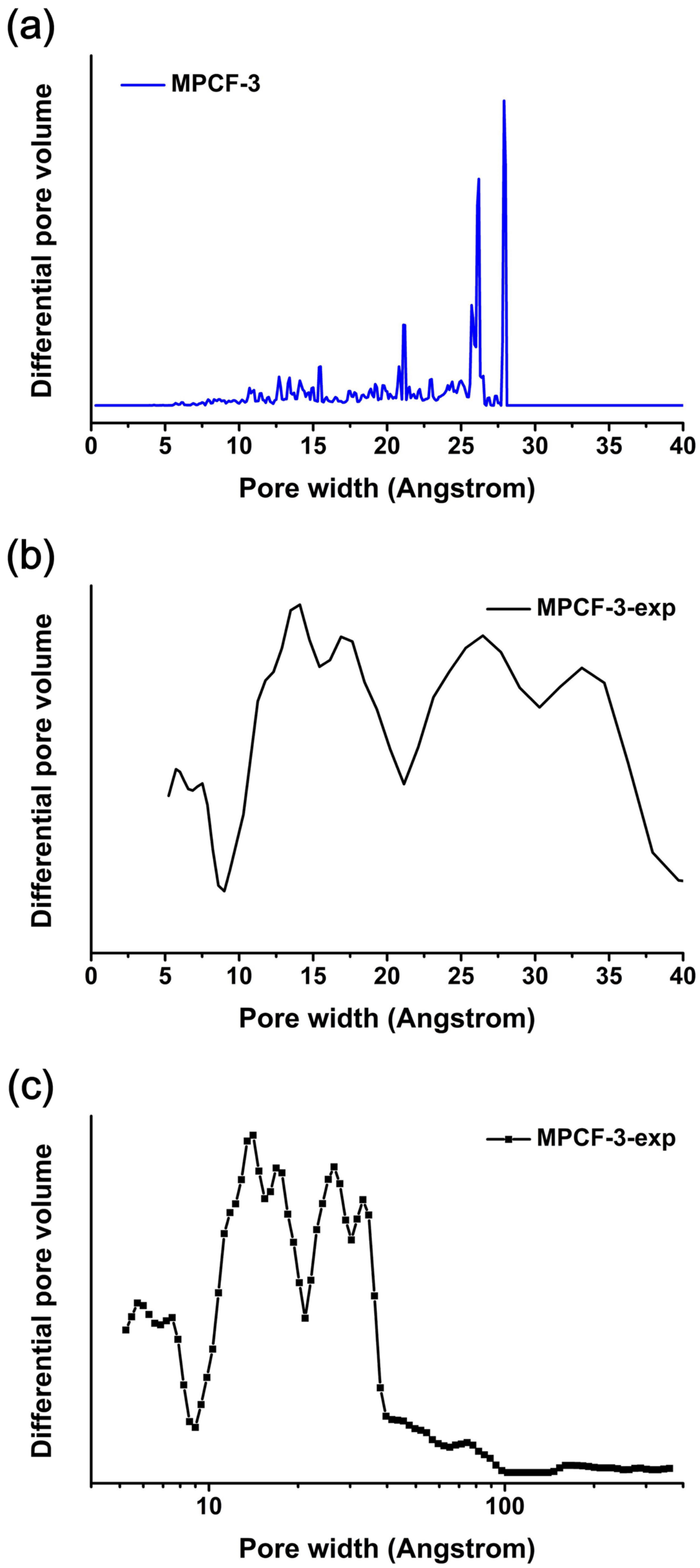

Fig. S13 (a) Simulated pore size distribution for the MPCF-3 model. (b, c) Experimental pore size distributions for MPCF-3 sample of different ranges for pore width.

7. Experimental synthesis of MPCF-3.

MPCF-3 was synthesized at 600 °C by ionothermal synthesis using $ZnCl_2$ as a catalyst and a solvent. Typically, OPBN (1.2 mmol, Fig. 1) and anhydrous $ZnCl_2$ (6 mmol) were mixed in a glovebox (argon with 0.1 ppm oxygen and 0.1 ppm water) and transferred to a quartz ampoule (Φ 20 mm x 150 mm). The ampoule was evacuated by vacuum, sealed and heated to 400 °C at a rate of 5 °C min^{-1} and maintained at this temperature for 6 h and then heated to 600 °C and held for 36 h. Subsequently, the internal compound was thoroughly washed with a 5% HCl solution, deionized water and tetrahydrofuran to remove $ZnCl_2$ and other impurities, then dried under vacuum at 100 °C for 12 h to obtain MPCF-3.

References

1. L. J. Abbott and C. M. Colina, *Macromolecules*, 2011, **44**, 4511-4519.
2. M. E. Fortunato and C. M. Colina, *SoftwareX*, 2017, **6**, 7-12.
3. C. Song, F. Hu, Z. Meng, S. Li, W. Shao, T. Zhang, S. Liu and X. Jian, *RSC Advances*, 2020, **10**, 4258-4263.
4. H. Sun, Z. Jin, C. Yang, R. L. Akkermans, S. H. Robertson, N. A. Spenley, S. Miller and S. M. J. J. o. m. m. Todd, 2016, **22**, 47.
5. R. L. Martin, B. Smit and M. Haranczyk, *Journal of Chemical Information and Modeling*, 2012, **52**, 308-318.
6. T. F. Willems, C. H. Rycroft, M. Kazi, J. C. Meza and M. Haranczyk, *Microporous and Mesoporous Materials*, 2012, **149**, 134-141.
7. S. Le Roux and V. Petkov, *Journal of Applied Crystallography*, 2010, **43**, 181-185.